Applied Physics A (2020) 126:917
https://doi.org/10.1007/s00339-020-04106-z

**Applied Physics A**
**Materials Science & Processing**

# Efficient, fast response, and low cost sensor for $NH_3$ gas molecules based on $SnO_2$: CuO/macroPSi nanocomposites

**Husam R. Abed[1] · Ali A. Yousif[2] · Alwan M. Alwan[3] · Nadir F. Habubi[2]**

Received: 23 June 2020 / Accepted: 23 October 2020 / Published online: 4 November 2020


**Abstract**
In the present study, a procedure of the inserting of $SnO_2$:CuO nanoparticles with different CuO nanoparticles contents within a macroporous silicon layer (macroPSi) gas sensor was prepared and successfully investigated. The macroPSi was effectively fabricated by laser assisted etching process, and CuO nanoparticles loaded with $SnO_2$ with a high value of surface area were successfully synthesized by the spray pyrolysis method. Atomic Force Microscopy (AFM) and Field Emission Scanning Electron Microscopy (FE-SEM) manifested a novel morphology for CuO Bucky particles inside the pores and a nano nail like structure for $SnO_2$ with a small average grain size of CuO Bucky particles with 30% content. This morphology of nanocomposites improved the sensing performance for $NH_3$ gas. A higher sensitivity with a very swift response and recovery times of 4 s and 55 s, respectively, was obtained with 150 ppm of $NH_3$ gas at the room temperature. This improvement in gas sensor performance is strongly related to the higher specific surface areas and smaller particle size with a higher surface roughness of $SnO_2$ and CuO nanoparticles within the nanocomposites.

**Keywords** Porous silicon · $NH_3$ sensor · $SnO_2$:CuO · Bucky particles · Spray pyrolysis

## 1 Introduction

Being the main source of contamination, ammonia gas ($NH_3$) is normally emitted as of organic decomposition, motor vehicles and manufacturing wastes [1]. Nevertheless, $NH_3$ is a harmful matter and could cause swelling for skin, and damaging for eye and lung. Thus, an $NH_3$ sensor with a great response that requires selectivity, high stability and a low detection threshold is important and immediately desirable. To understand this, researchers have completed many of the works and elaborated a diversity of sensitive materials [2–8]. Conversely, most of them are essential to be worked at the elevated temperatures owing to their low electrical conductivity at the room temperature (RT), which is uncomplimentary for power saving, sensor assimilation and thermal stability [9]. So, it is essential to improve an inexpensive, sensitive, fast and dependable ammonia gas sensor, which is still a confrontation for the familiar materials for gas sensing. Metal oxide semiconductor (MOS) was established, presented the cost effectiveness and improved the sensing performance as a profound sample in the species of a continuous layer or cluster landmasses [10–14]. For example, tin dioxide ($SnO_2$) sample was prepared with copper oxide (CuO) nanoparticles [11, 12, 14]. Kumar et al. [15] have coated $SnO_2$ and $SnO_2$/CuO bilayer films straight on porous anodic alumina, the gas response (defined by $R_a/R_g$) toward 100 ppm of $NH_3$ gas was about 3.2 at 180 °C. Li et al. [16] have studied the gas sensor performance based on $SnO_2$:CuO deposited on silicon substrate, they observed that the sensitivity toward 100 ppm of $NH_3$ gas molecules was about 54% using the formula $((R_g - R_a)/R_a) \times 100$. Eom et al. [17] have synthesized $SnO_2$:$Cu_2O$ nanocomposite on glass substrate, they found that the sensitivity ($R = (\Delta R/R_g) \times 100\%$) towards 200 ppm of $NH_3$ is about 4% at the room temperature. Bo et al. [18] have prepared $SnO_2$:CuO on graphene sheet, they reported that the sensitivity ($R = (\Delta R/R_g) \times 100\%$) is 16% towards 50 ppm of $NH_3$ gas. The prospective of the proposed porous silicon (PSi)

✉ Nadir F. Habubi
nadirfadhil@uomustansiriyah.edu.iq

[1] The General Directorate for Education in the Province of Baghdad - Rusafa / 2, Ministry of Education, Baghdad, Iraq

[2] College of Education, Mustansiriyah University, Baghdad, Iraq

[3] Department of Applied Sciences, University of Technology, Baghdad, Iraq

excessive was used as gas sensor elements at the room temperature because of their amazing feature; a high specific surface area. Also, it has been described that the existence of $NH_3$, $NO_2$, $O_2$ gases molecules and other gases can alter the conductivity of PSi layer [19, 20]. Thus, the aim of the current research is to boost the performance of the gas sensing based on a porous silicon layer by inserting of $SnO_2$:CuO nanoparticles with different contents of CuO nanoparticles within a macroporous silicon layer (macroPSi). The content of CuO nanostructures was adjusted for the promoted response merits towards the ammonia ($NH_3$) gas molecules.

## 2 Experimental work

### 2.1 PSi materialization

The n-type of silicon wafers substrates with an orientation (100) and a resistivity of 10 Ω. cm were used for the PSi fabrication. A 6 min dip in 10% HF was used to remove the surface native oxide. The laser-assisted method based on the combination solution of the etching process of 1:1 of ethanol (99.999 purity) and 40% of hydrofluoric acid was used to form the PSi layer. The current density of about 12 mA/cm$^2$ of the etching process was fixed for 15 min, and the used laser has a 640 nm wavelength with the intensity of 50 mW/cm$^2$. The setup of experimental work (Fig. 1) composed of: ammeter, photon source, suitable homemade HF resistance etching cell consists of Teflon as a container for HF solutions and fitting aluminum as an electrode for conducting the current to the bottom silicon surface, and the platinum electrode (immersing in solution) utilized as cathode. All these requirements are considered as effective parameters in laser-assisted method. Following the etching method, the porous silicon layer was cleaned by deionized $H_2O$ and then dried for a few minutes in the atmosphere. The porosity of porous silicon was obtained by the following equation [21]:

$$P = (M_1 - M_2)/(M_1 - M_3) \quad (1)$$

where $M_1$, the mass of the PSi film before anodization route, $M_2$, the mass of the PSi film after anodization technique, and $M_3$, the mass of the sample after eliminating the PSi surface utilizing the KOH solution.

### 2.2 Elaboration of the nanocomposite films

Afterward, the etching step was completed, the spray pyrolysis technique was used to deposit the nanoparticles on the porous silicon layer. The experimental set-up of the spray pyrolysis method comprises a solution, which was sprayed on the surface of porous silicon at 400 °C, where the reaction of the solution led to the synthesized optimal nanoparticles. The solution that used in this method consists of 0.1 M $CuCl_2$ (by BDH, from ENGLAND) and 0.1 M $SnCl_4{\cdot}5H_2O$ (by BDH, from ENGLAND), different samples of (bare PSi, pure $SnO_2$, 50%$SnO_2$:50%CuO, 90%$SnO_2$:10%CuO, and 70%$SnO_2$:30%CuO) were fabricated with a 50 ml of the solution for each deposition process. The ideal parameter conditions for the spray pyrolysis method were detected by employing a plastic atomizer with a nozzle having an outlet of about 0.9 mm, and the spraying time was 7 s with an interval time of 70 s under a constant pressure of 2.5 bar. The

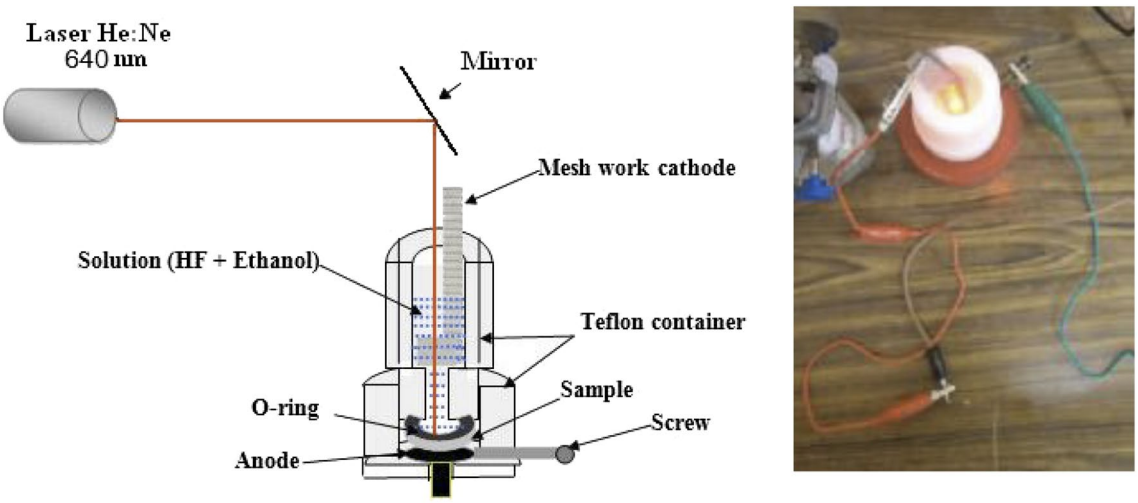


**Fig. 1** Experimental set-up of laser-assisted etching process

flow rate of the spray was about 2.2 ml/min, and the distance between the sample and the nozzle was fixed at 20 cm.

### 2.3 Gas sensing characterization

The morphological aspects of $SnO_2$:CuO/PSi Nanocomposites were examined via field emission scanning electron microscopy (FE-SEM) (INSPECT-550) and atomic force microscope (CSP model AA3000 AFM supplied by Angstrom Company). The chemical elements were investigated by electron dispersive spectroscope (EDS) (INSPECT-550). The crystal structure of porous silicon was provided by the X-ray diffract meter (Shimadzu 6000) via CuKα ($\lambda = 1.54056$ Å) radiation. The $NH_3$ sensing performance was done in a chamber system consisting of an adjustable heat plate, a digital program readout system, and a glass cavity. The ohmic contact made of aluminum was deposited on the surface of the sample by thermal evaporation method using a mask of grid shape with a thickness of (25 nm). Figure 2 displays the representation of the gas sensing set-up. Throughout the test, the $NH_3$ gas was introduced into the chamber, and the variation in the electrical resistance was measured at a fixed voltage of 5 V. The relative humidity was 32%, and the chamber dimensions are $1 \times 1 \times 1$ $m^3$. Different cylinders of ammonia were used to obtain various concentrations.

## 3 Results and discussion

### 3.1 Morphological features

The morphology and the cross-sectional images of the surface of macroPSi, $SnO_2$/macroPSi, and $SnO_2$:CuO/macroPSi are investigated by FE-SEM, Fig. 3. Figure 3a depicts that the structure of macroPSi consists of non-completed pores, irregular and semi-cubic shapes, this is because of the overlapping of pores among the specific non-completed pores, and the macropores are randomly distributed over the layer. This process of overlapping among the pores under the fabrication path takes place because etching is a three-dimensional route with various etching rates [22]. The pore diameters have a range of about (0.35–4.8) µm and the average diameter is 2.82 µm. The porosity of macroPSi layer is about 71.6%. For the $SnO_2$/macroPSi nanocomposite structures revealed in Fig. 3b, the appearances of $SnO_2$ nanostructures that deposited on the surface of macroPSi are semi-cubic with particle sizes in the range of (82–100 nm). The morphological structure of $SnO_2$:CuO/macroPSi nanocomposites with different concentrations of CuO is shown in Fig. 3c, and e, from these figures, one can notice that the $SnO_2$:CuO nanostructures have a semi-spherical structure and the $SnO_2$ particles have a nano nail-like shape on the walls of the pores. Figure 3d evinces a novel morphology for the CuO Bucky particles inside the pores and a nano

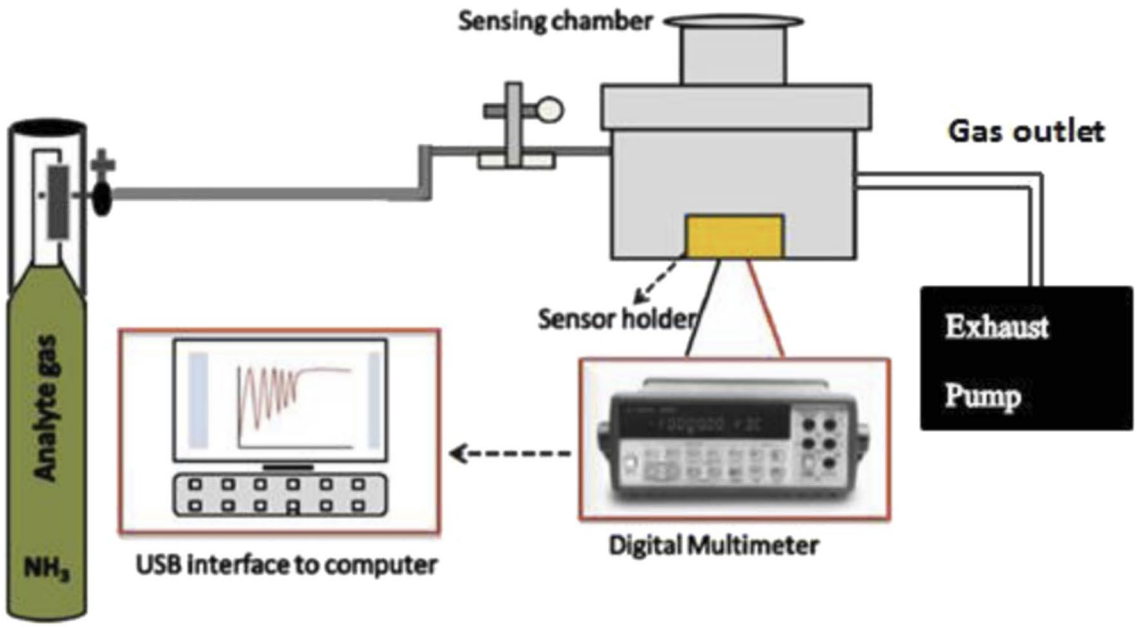


**Fig. 2** Representation of the gas sensing set-up

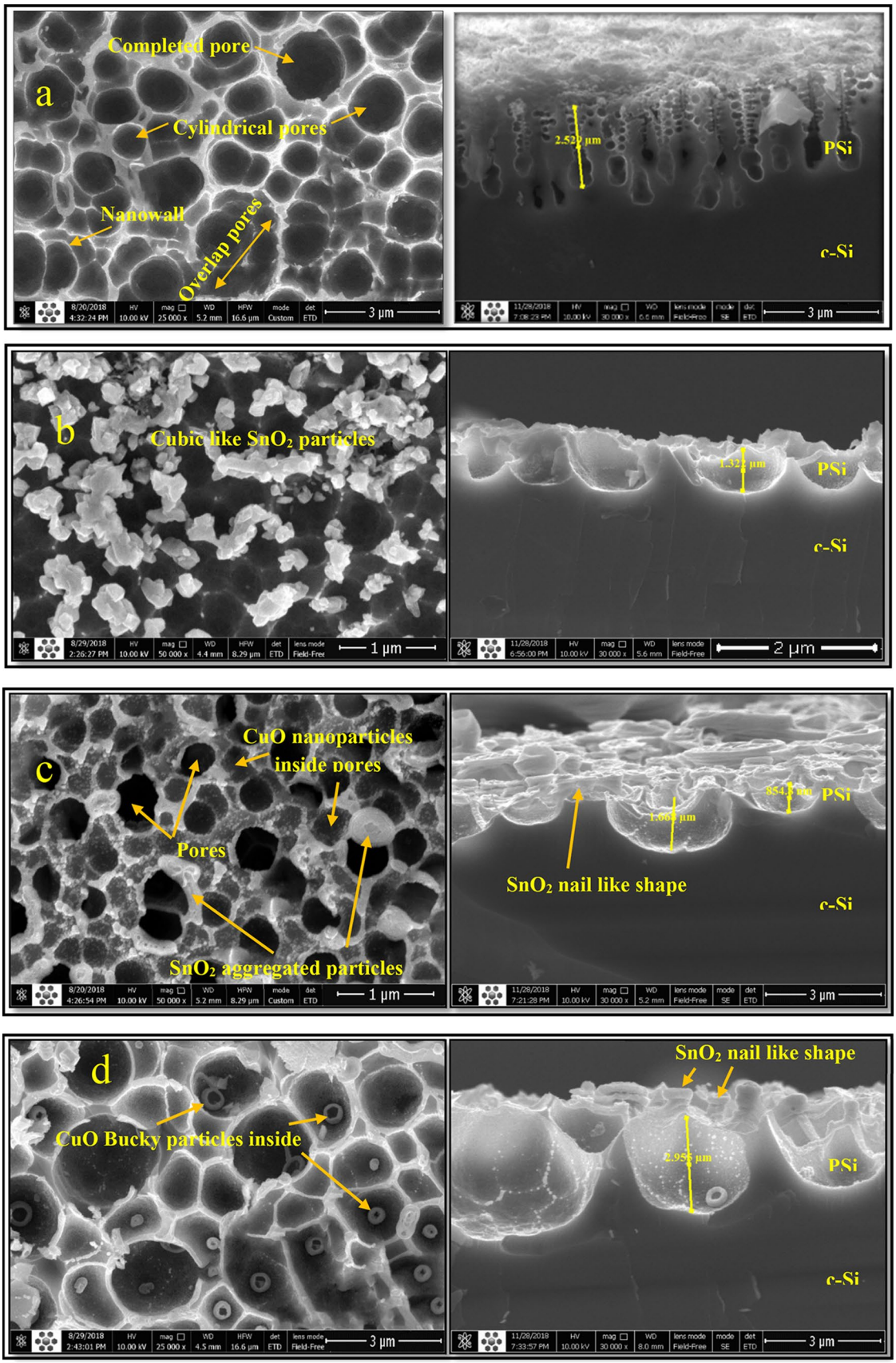


**Fig. 3** FE-SEM images with cross section of **a** macroPSi, **b** un-mixed $SnO_2$, **c** 10%CuO:90%$SnO_2$, **d** 30%CuO:70%$SnO_2$, and **e** 50%CuO:50%$SnO_2$

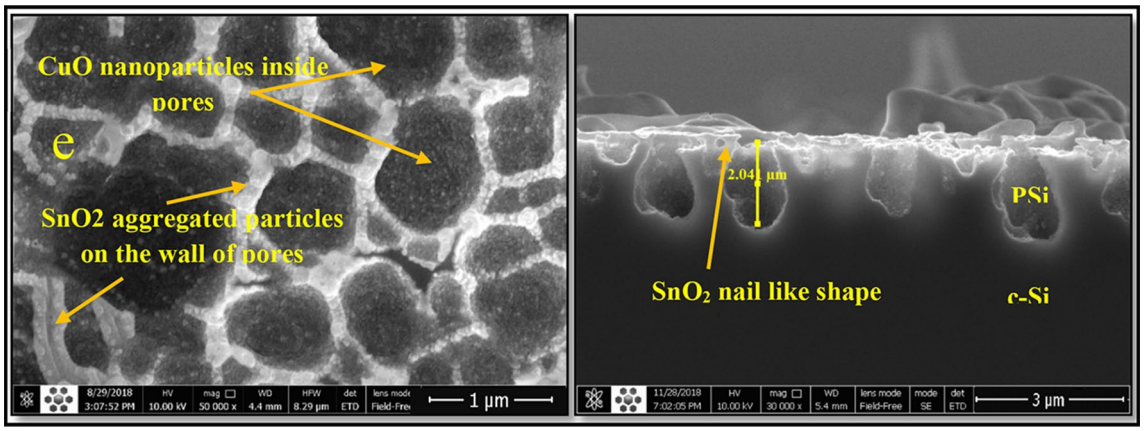


**Fig. 3** (continued)

nail-like structure for $SnO_2$. A great number of nanoparticles are aggregated on the walls of the macroPSi, and the others of CuO nanoparticles are inside the macroPSi, this is in compatibility with [23]. By increasing the CuO nanoparticles content from 10 to 30%, the sizes of the nanoparticles decreased from 95 to 37 nm with enhancing the surface homogeneity, and for 50% content they returned to increase to 45 nm. From these results, it can be concluded that by monitoring the content of the copper oxide nanoparticles, the surface area over macroPSi layer will be improved.

The $SnO_2$:CuO nanoparticles elements were investigated by the spectra of EDS, as demonstrated in Fig. 4a–d. The existence of $SnO_2$:CuO nanoparticles was confirmed by the appearance of elements Si, Cu, Sn, and O without any impurities. Moreover, it can be observed that as the CuO nanoparticles content increased, the peak of it increased within the $SnO_2$:CuO nanoparticles. The elemental maps for Si, O, Sn, and Cu is displayed in Fig. 4e–h. The spreading of the elements of O, Si, Sn, and Cu clearly distinguishes the $SnO_2$ from CuO ones.

### 3.2 Atomic force microscopy analysis

The topographical characteristics of $SnO_2$/macroPSi and $SnO_2$:CuO/macroPSi nanoparticles are elucidated in Atomic Force Microscopy pictures in Fig. 5. The AFM pictures confirm that the surfaces of the samples have a great degree of homogeneity. The root mean square (RMS) and the roughness of the surface are increased by increasing the CuO nanoparticles content, as depicted in Table 1. From this table, the highest value for the average roughness is (54.5 nm) and the lowest value for average grain size is (40.26 nm), which correspond to the CuO nanoparticles content of 30%. The granularity size distribution of the fabricated nanoparticle size, as presented in Fig. 5, emphasizes that the surface properties of the nanoparticles are varying according to the controlled content of CuO nanoparticles. As the particles sizes decreased to the lowest possible values the physical system under measurement reach to the nano regime boundaries and hence the expected vacancies within the topographical patterns will increase and hence the roughness is increased.

### 3.3 XRD analysis

Figure 6 manifests the peaks of the $SnO_2$/macroPSi and the $SnO_2$:CuO/macroPSi nanostructures analyzed by XRD. In Fig. 6d, the diffraction peaks at 26.6, 33.8, 37.9, 51.7, 54.7, 61.8, 78.7, 83.7, and 90.8 correspond to the (110), (101), (200), (211), (220), (310), (321), (222) and (411) phases of tetragonal $SnO_2$ structure (PDF# 41-1445), respectively. In Fig. 6b and c, the diffraction peaks at 35.4 and 38.7 correspond to the (002) and (200) phases of monoclinic CuO, respectively, which were reliable with (PDF# 48-1548). The patterns that diffracted from the XRD were recognized to the typical $SnO_2$ and CuO peaks, and no peaks were detected for other materials. In Fig. 6, the $SnO_2$ and CuO peaks were widened. This is due to the poorer crystallization ratings of the film, which is related to the defects that arise from the spray pyrolysis technique, also the addition of impurities decreased the crystallization ratings [24]. From the XRD patterns, it can be noted that the average nanocrystal size decreased with the increasing of CuO nanoparticles content within the $SnO_2$:CuO nanoparticles, therefore, the surface area will develop by the modification of CuO nanoparticles with the $SnO_2$ nanostructure. Table 2 lists the surface area and the average nanocrystal size. The highest specific surface area, the largest amount of gas response for gas sensing performance.

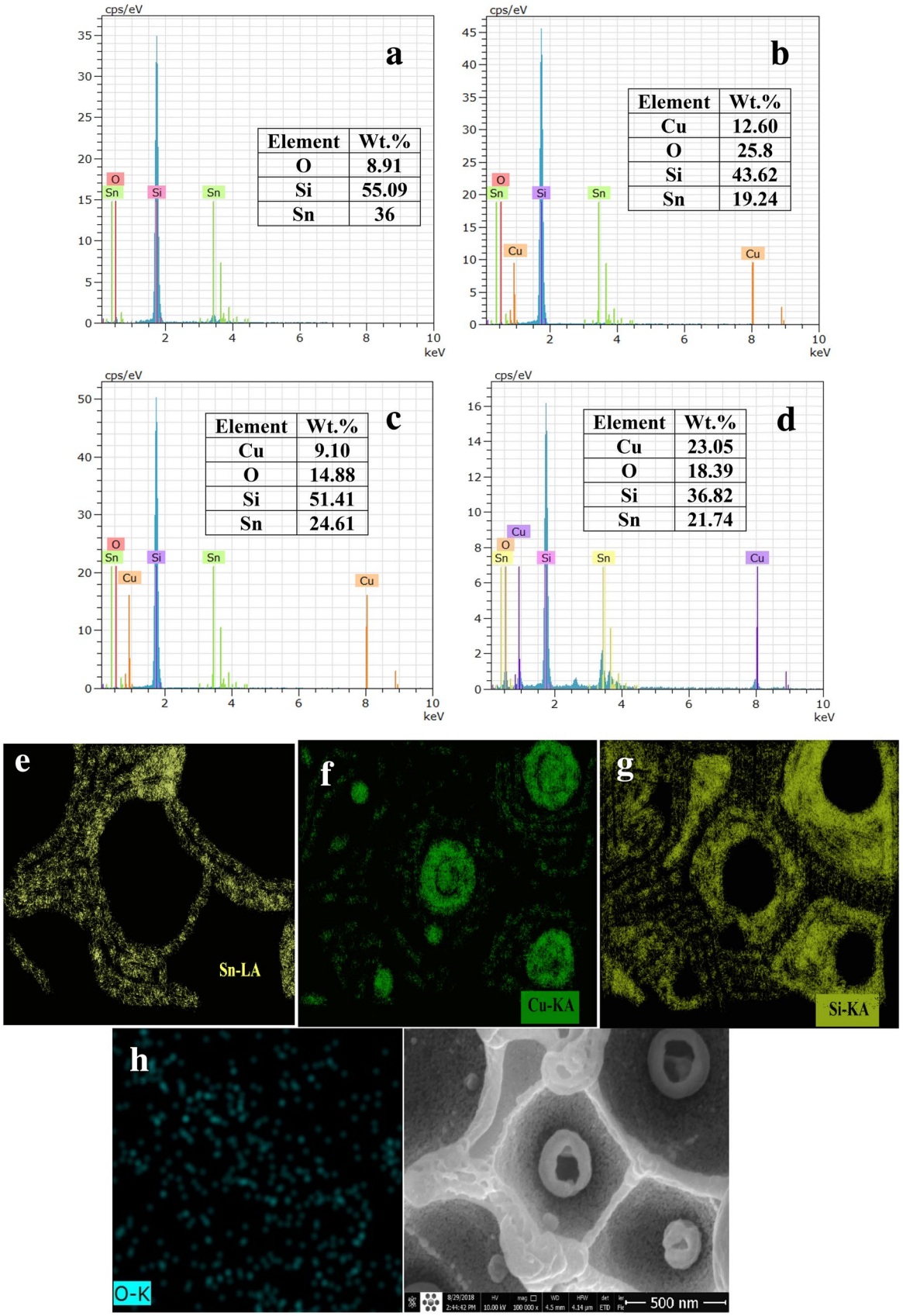
a
cps/eV
keV
O
Sn
Si
Sn
Element Wt.%
O 8.91
Si 55.09
Sn 36
b
cps/eV
keV
O
Sn
Si
Sn
Cu
Cu
Element Wt.%
Cu 12.60
O 25.8
Si 43.62
Sn 19.24
c
cps/eV
keV
O
Sn
Si
Sn
Cu
Cu
Element Wt.%
Cu 9.10
O 14.88
Si 51.41
Sn 24.61
d
cps/eV
keV
Cu
O
Sn
Si
Sn
Cu
Element Wt.%
Cu 23.05
O 18.39
Si 36.82
Sn 21.74
e
Sn-LA
f
Cu-KA
g
Si-KA
h
O-K
500 nm

◂**Fig. 4** Electron dispersive spectra **a** un-mixed $SnO_2$, **b** 10%CuO:90%$SnO_2$, **c** 30%CuO:70%$SnO_2$, **d** 50%CuO:50%$SnO_2$, whereas **e**–**h** is the element map for 30%CuO:70%$SnO_2$

The average crystallite size $D$ was calculated using the Scherrer formula given by Eq. 2 [25].

$$D = (0.94\lambda)/[\beta_{(2\theta)}\cos\theta] \quad (2)$$

where, the wavelength of XRD is $\lambda$, the full width at half maximum of diffracted peaks is $\beta_{(2\theta)}$, and $\theta$ is the Bragg angle.

The specific surface area (S.S.A) of $SnO_2$:CuO nanoparticles was obtained by Sauter formula [26]:

$$\text{S.S.A} = 6000/(D * \rho_{\text{d}}) \quad (3)$$

where, $\rho$ is the density of $SnO_2$:CuO nanoparticles, the Sauter's formula involves a 'shape factor' which is 6 for the sphere.

### 3.4 Electrical properties

Current–Voltage characteristics were investigated under the dark condition and the different ammonia gas concentrations (50, 100, and 150) ppm and temperatures (room temperature (RT), 50, 75, and 100) $^{o}$C, as shown in Fig. 7. All samples demonstrated that the current increased with the increasing of gas concentration and temperature. All the samples showed an ohmic contact for the bare PSi and modified PSi, this is due to the double junction: PSi/n-Si and $SnO_2$:CuO, and the barrier height of the first junction could be in opposite direction to the second junction. One of the most important behaviors for the gas sensor property is the ohmic contact; this is related to the affected sensitivity of the sensor device by contact resistance and could be highly changed when introduced to the $NH_3$ gas molecules. The same behavior was found by [27] for Au modified PSi, and also [17] obtained the ohmic behavior for $SnO_2$, $SnO_2$:CuO, and $SnO_2$:$Cu_2O$. The elevated resistance for the CuO loaded with $SnO_2$ proposes that the depleted electrons of p–n junction were favorably created from the tin dioxide layer and are more effective than the oxygen adsorption [28]. Also it should be mentioned that there are two types of defects for the CuO dopant that could affect the resistance of the film. The first is the substitution defect, in which the $Cu^{2+}$ could substitute $Sn^{4+}$ this will increase the oxygen vacancy, and hence decrease the free electrons and increase the resistance. The second is the interstitial defect, in which the copper ions could occupy the interstitial positions in $Sn^{4+}$, this will lead to the decreasing of oxygen vacancy and hence increasing the free electrons and the resistance of the sensor. Table 3 lists the resistance obtained from the current–voltage characteristics.

### 3.5 Gas sensing measurement

The sensing features of bare porous silicon, $SnO_2$ and $SnO_2$:CuO/macroPSi nanocomposites were recorded to clarify the consequence of altering the CuO nanoparticles on the fabricated sensor. The measurement was repeated three times to confirm the obtained results. The FE-SEM images revealed that the CuO nanoparticles and Bucky particles inside the pores of macroPSi as well as the high specific surface area enhanced the response, which might offer additional adsorption locations for gas molecules. Furthermore, the suitable pore dimensions of (0.35–4.8 µm) might store the $NH_3$ molecules provisionally to interrelate with the sensing element entirely. Figures 8a–e demonstrates that the resistance of the bare PSi, $SnO_2$/macroPSi, and $SnO_2$–CuO/macroPSi nanocomposite sensors varies with the interval upon experience to several $NH_3$ gas concentrations (50, 100, and 150) ppm at different temperatures (RT, 50, 75, and 100) °C. All the $SnO_2$–CuO/macro-PSi nanocomposites sensors showed a good reversible response. The CuO content enhanced the response to ammonia gas. In particular, the $SnO_2$–CuO/macroPSi nanocomposites sensors responded to ammonia gas at the RT. After the exposure to $NH_3$ gas, the resistance decreased and reverted to the previous case upon the exposure to air which corresponds to the typical n-type semiconducting behavior [29]. Figure 8a evinces a good response of macroporous silicon at all investigated temperatures, fast response time and recovery time at the RT, and when the temperature reached to 50 °C, the response and recovery times increased and so on at 75 °C, but at 100 °C, they became lower. Figure 8b illustrates that the $SnO_2$ nanostructures have developed the sensitivity. The response time and recovery time get faster than that in macro-PSi at the RT. When the CuO nanoparticles incorporated with 10% to 90% $SnO_2$, the response to ammonia improved at the RT and 50 °C with very fast response and recovery times. In Fig. 8d, as the content of CuO increased to 30%, the ideal response and recovery times obtained, especially at the RT as shown in Fig. 9, this could be attributed to the morphology of the copper oxide Bucky nanoparticles (Fig. 4d) inside the pores of PSi, high specific surface area, and particle size that boosted the response to $NH_3$ gas. This is in agreement with

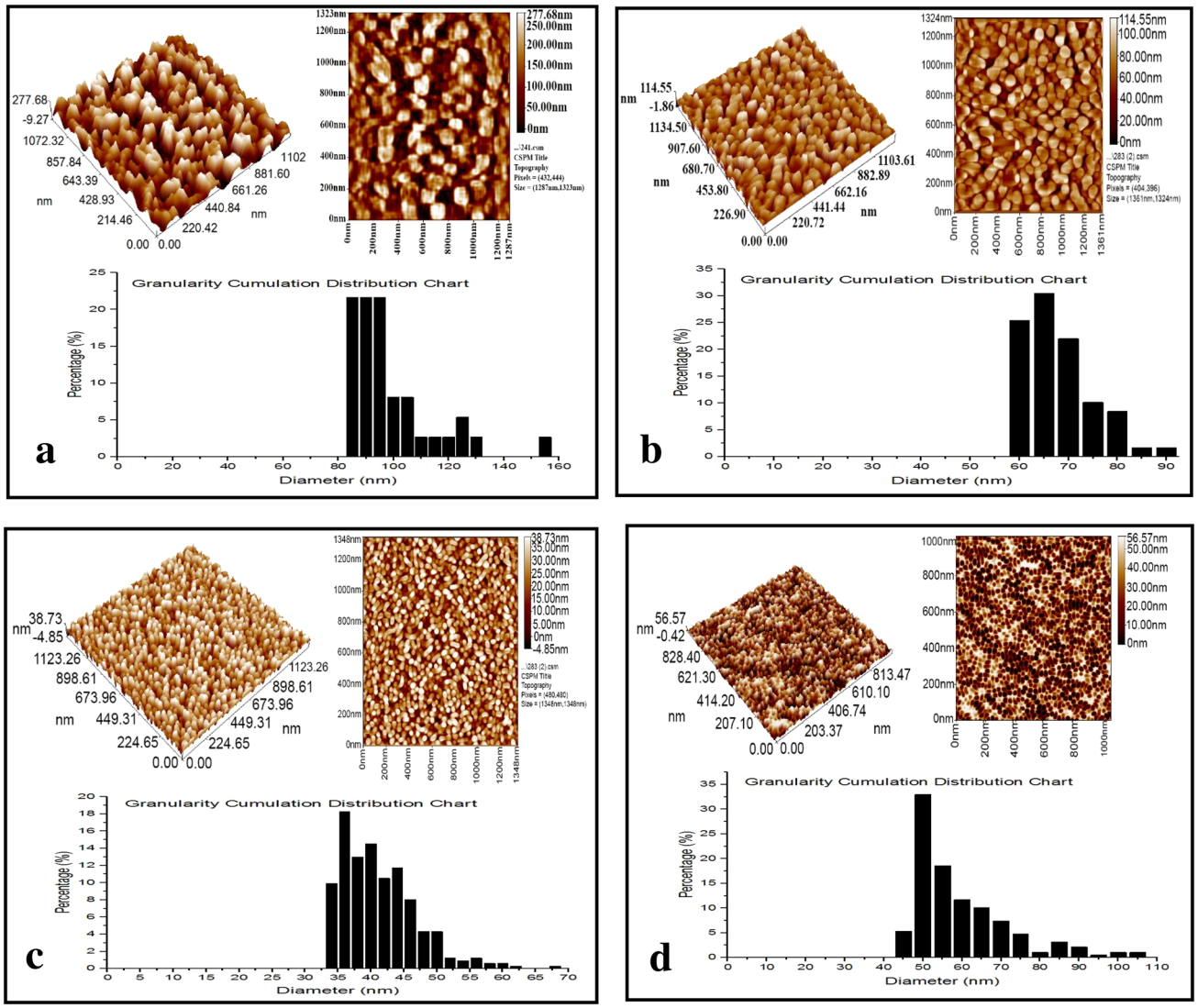


**Fig. 5** Two-Dimension and 3-Dimension AFM images of **a** Pure $SnO_2$, **b** 10%CuO:90%$SnO_2$, **c** 30%CuO:70%$SnO_2$, **d** 50%CuO:50%$SnO_2$

**Table 1** Roughness parameters and average grain size

| Sample | Root mean square (nm) | Roughness (nm) | Average grain size (nm) |
|---|---|---|---|
| Pure $SnO_2$ | 45 | 39 | 96.47 |
| 90% $SnO_2$: 10% CuO | 48.6 | 42.1 | 65.5 |
| 70% $SnO_2$: 30% CuO | 63.2 | 54.5 | 40.26 |
| 50% $SnO_2$: 50% CuO | 47.3 | 40.8 | 57.2 |

those that reported the effect of the morphology and particle size on the gas sensing performance [30, 31]. The response and recovery times become little higher when 50% CuO nanoparticles loaded to 50% $SnO_2$, this is due to the low specific surface area as illustrated in Table 2, which shows the great grain size, consequently the perfect response is prominent with 30% CuO Bucky particles content. The sensitivity is the maximum at the RT (25 °C) and it reduces with the elevated temperatures. The detected drop in the sensitivity might be linked to the shrinking sample resistance in air which is

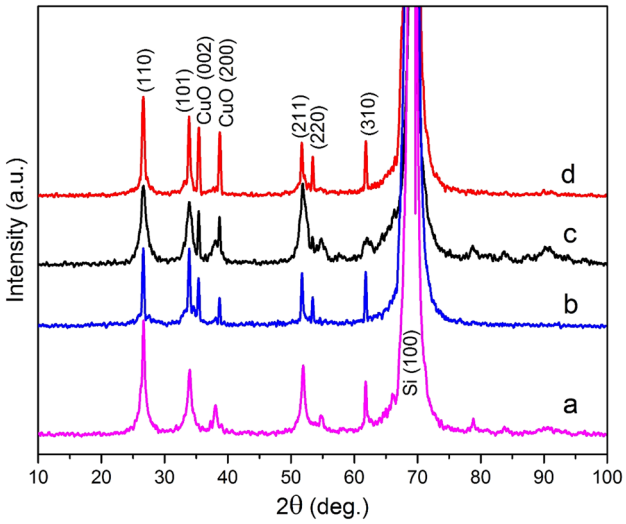


**Fig. 6** X-Ray Diffraction patterns of; **a** $SnO_2$, **b** 10%CuO:90%$SnO_2$, **c** 30%CuO:70%$SnO_2$ and **d** 50%CuO:50%$SnO_2$

initiated from the improvement in the phonon assisted tunneling that results in dropping resistance [32]. Meanwhile, the developed structure in this work comprises relatively an extra density of O vacancies, and the diverse variation in the resistance of sensor with the elevating temperature appears reasonable. The noise in the sensor device could be attributed to many reasons, such as the thermal motion of electrical charges, the amplifier in locally manufactured gas sensor system, and Brownian motion which caused by the irregular forces arise from the random collisions of molecules in the low size particles. The last one comes to be more important when the size of a structure reduces. The noise in chemical sensors (adsorption–desorption processes) is related to the Brownian motion [33]

Figure 10 indicates that the sensitivity as a function of temperature at 150 ppm gas concentration of macro PSi is good, but it decreases as the temperature increases. Sensitivity gets enhanced for $SnO_2$ nanostructure to 37%. When the CuO nanoparticles were incorporated with 10%, the sensitivity improved at the room temperature with the value of 47%. The excellent sensitivity obtained when 30% CuO Bucky particles was loaded, it showed 57% of sensitivity at room temperature. As the CuO nanoparticles content was increased to 50%, the sensitivity fell back to 31% at the room temperature. All samples exhibited a perfect response at the room temperature, and the temperature, in which the sensitivity displays a supreme rate, is named the best working temperature. Conversely, if the working temperature rises more than the room temperature, the response will drop as the extent of the adsorbed ammonia gas on the nanocomposite internal exposure surface drops. Whereas, the desorption rate becomes principal with the growing working temperature, leading to a drop in response. Table 4 lists the response time, recovery time, and the sensitivity of the ammonia gas, and Table 5 illustrates the performances of various categories of nanocomposites sensors. The sensitivity of the gas sensor was calculated by the following equation [34]:

$$\text{Sensitivity} = \frac{R_a - R_g}{R_a} \times 100\% \quad (4)$$

where, $R_g$ is the measured resistance at the presence of ammonia gas molecules, and $R_a$ is the resistance at the absence of ammonia gas molecules.

**Table 2** Average values of the nanocrystal size and the specific surface area

| Sample | Main plane | 2$\theta$ (deg.) | Average nanocrystal size (nm) | Specific surface area ($m^2$/gm) |
|---|---|---|---|---|
| Pure $SnO_2$ | 110 | 26.6 | 26 | 33 |
| 90% $SnO_2$:10% CuO | 110 | 26.62 | 19 | 45 |
| 70% $SnO_2$:30% CuO | 110 | 26.68 | 10 | 86 |
| 50% $SnO_2$:50% CuO | 110 | 26.69 | 13.2 | 65 |
| 90% $SnO_2$:10% CuO | 002 (CuO) | 35.47 | 16 | 59 |
| 70% $SnO_2$:30% CuO | 002 (CuO) | 35.41 | 9.2 | 103 |
| 50% $SnO_2$:50% CuO | 002 (CuO) | 35.43 | 12 | 79 |

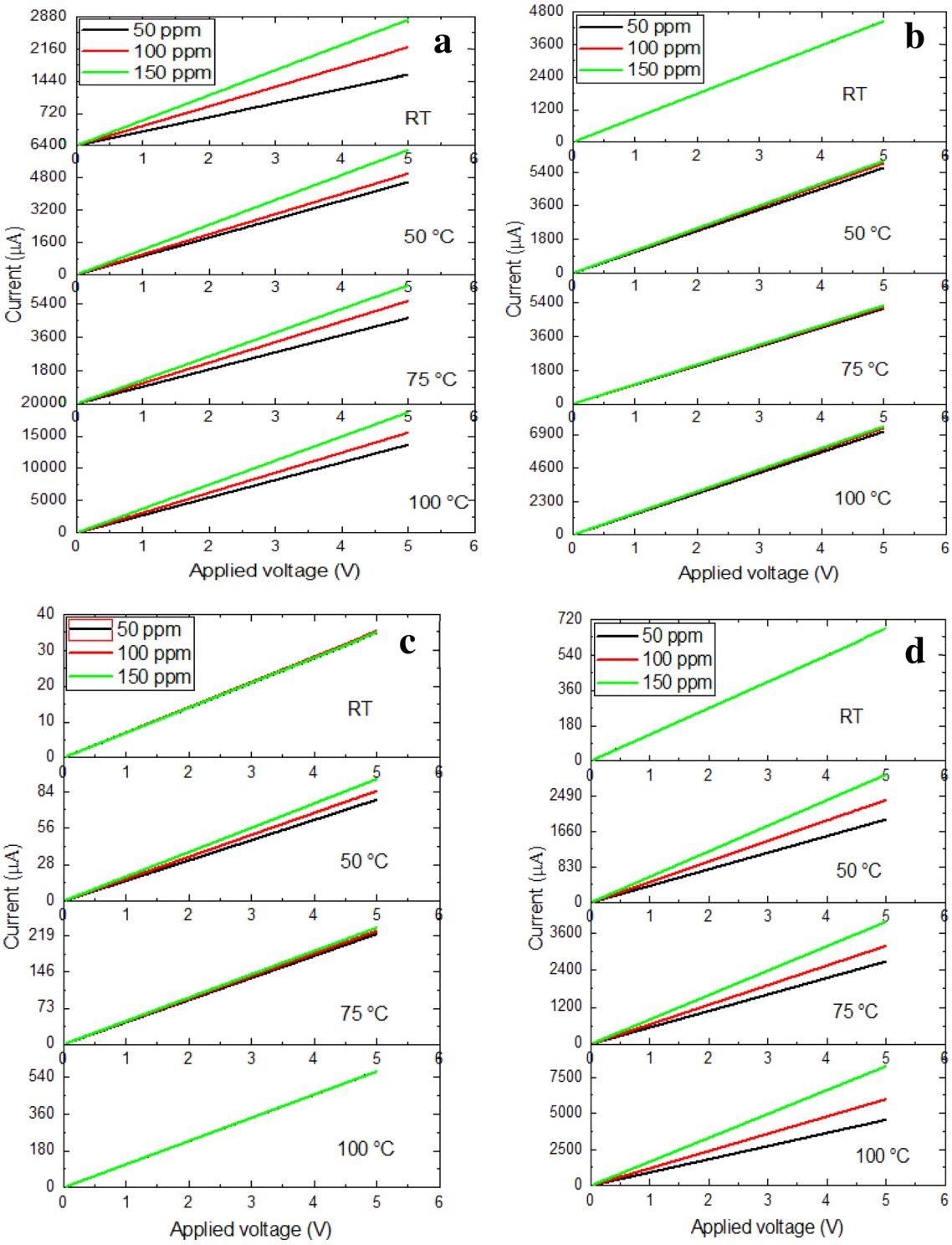


**Fig. 7** Current–Voltage characteristics for **a** PSi, **b** $SnO_2$, **c** 90% $SnO_2$:10%CuO, **d** 70% $SnO_2$:30%CuO, and **e** 50% $SnO_2$:50%CuO

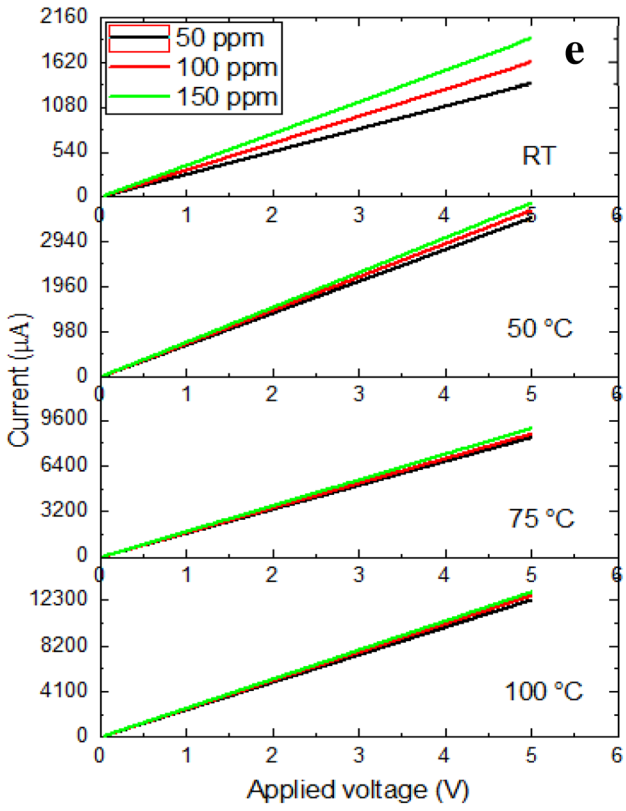


**Fig. 7** (continued)

## 4 Conclusion

Briefly, the inserting of $SnO_2$:CuO nanoparticles with different CuO nanoparticles contents deposited over photo electrochemically etched macroporous silicon represents an efficient route for developing a gas sensor. The 30% CuO content manifested larger specific surface area and smaller particle size with higher roughness surface than pure $SnO_2$ and other CuO contents, as obtained from the XRD and AFM. FE-SEM revealed a pore depth of 2.5 μm with various pore diameters in the range (0.35–4.8 μm), and the porosity of the macroPSi was 71.6%. The $NH_3$ gas sensor based on $SnO_2$:CuO/macroPSi nanocomposite elucidated an extra sensitive performance, 4 s response time and 55 s recovery time of 4 s, especially when 30% CuO was loaded to 70% $SnO_2$, it evinced a 57% of sensitivity at the room temperature. The high sensitivity of the nanocomposite is credited to its level of crystallinity, additional oxygen vacancies, and heterojunction creation. Consequently, $SnO_2$:CuO/macroPSi nanocomposites with the improved sensitivity have a high probability in the $NH_3$ sensor presentations.

**Table 3** Resistance of PSi, $SnO_2$, and $SnO_2$:CuO deposited on the etched n-Si

| Material | Temperature (°C) | Gas concentration (ppm) | Resistance (Ω) |
|---|---|---|---|
| PSi | RT | 50 | 3174 |
| | | 100 | 2288 |
| | | 150 | 1785 |
| $SnO_2$ | RT | 50 | 1126 |
| | | 100 | 1125 |
| | | 150 | 1124 |
| 90% $SnO_2$:10% CuO | RT | 50 | 166,666 |
| | | 100 | 142,857 |
| | | 150 | 142,855 |
| 70% $SnO_2$:30% CuO | RT | 50 | 7462 |
| | | 100 | 7461 |
| | | 150 | 7460 |
| 50% $SnO_2$:50% CuO | RT | 50 | 3676 |
| | | 100 | 3095 |
| | | 150 | 2631 |

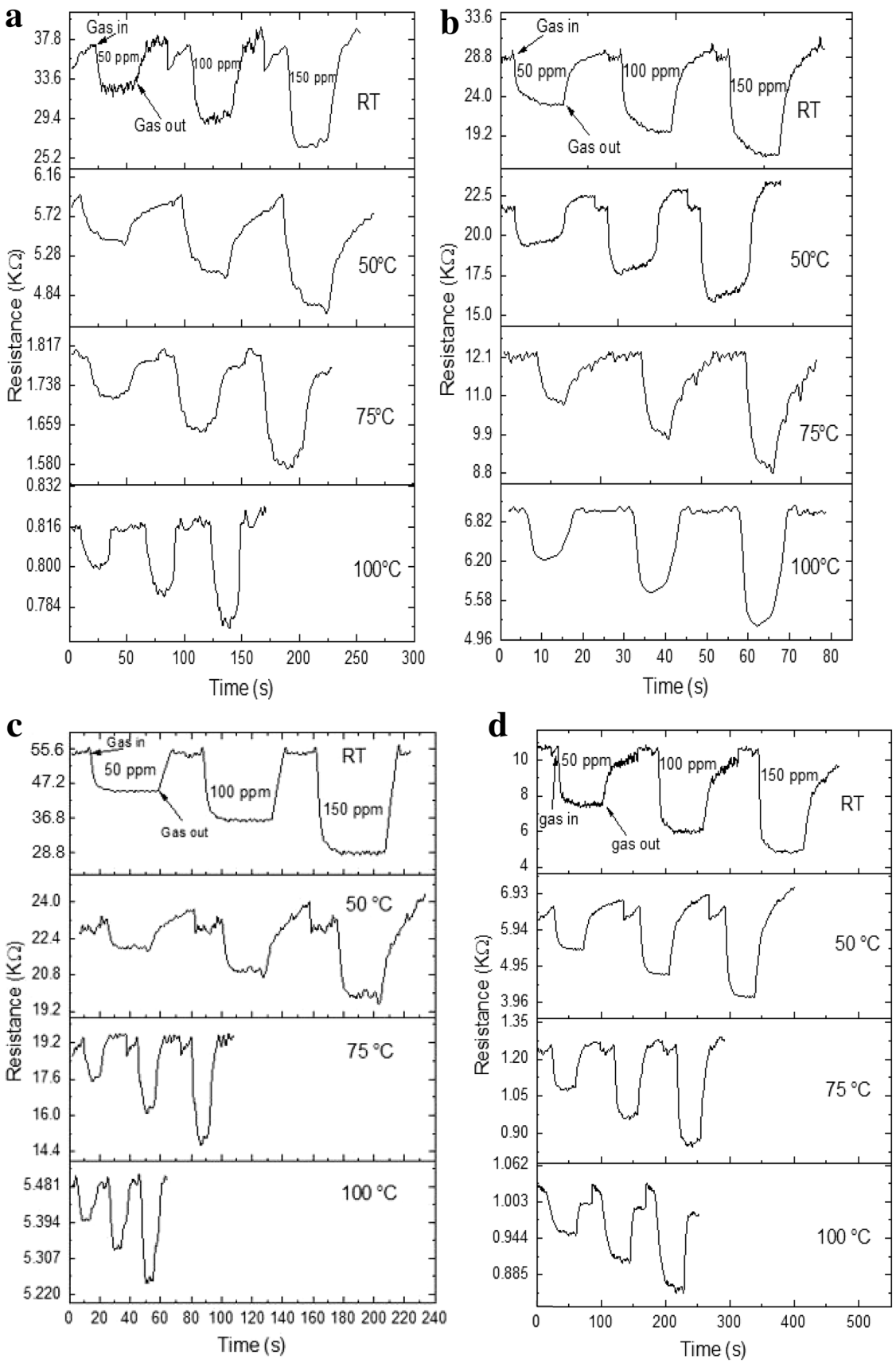


**Fig. 8** Resistance change as a function of time when introduced to different ammonia concentrations at various temperatures of **a** macro PSi, **b** $SnO_2$, **c** 10% CuO:90% $SnO_2$, **d** 30% CuO:70% $SnO_2$, and **e** 50% CuO:50% $SnO_2$ nanocomposites sensors

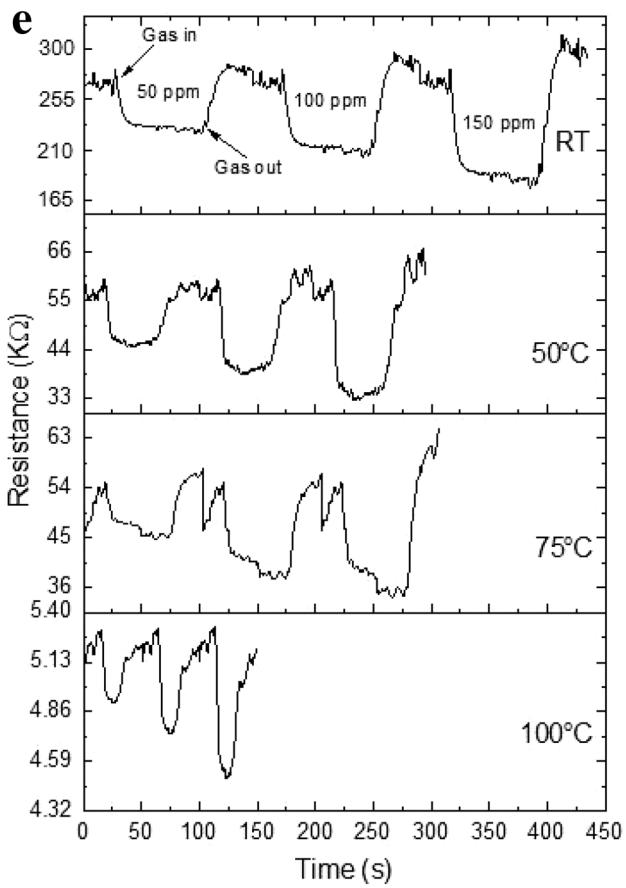


**Fig. 8** (continued)

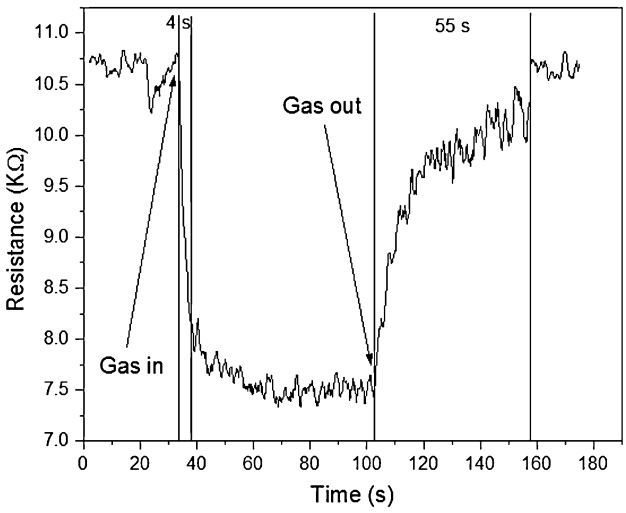


**Fig. 9** Response and Recovery times for 50 ppm $NH_3$ gas of nanocomposites sensors 70% $SnO_2$:30% CuO/macro-PSi at room temperature

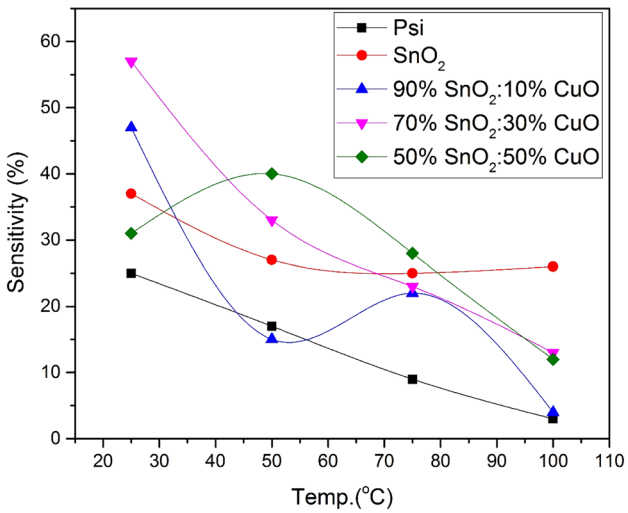


**Fig. 10** The sensitivity as a function of temperature at 150 ppm of ammonia gas

**Table 4** Response time, recovery time, and sensitivity to 150 ppm of $NH_3$ gas at the RT

| Sample | Response time (S) | Recovery time (S) | Sensitivity (%) |
|---|---|---|---|
| Macro PSi | 10 | 70 | 25 |
| $SnO_2$ | 8 | 64 | 37 |
| 90% $SnO_2$:10% CuO | 7 | 58 | 47 |
| 70% $SnO_2$:30% CuO | 4 | 55 | 57 |
| 50% $SnO_2$:50% CuO | 10 | 50 | 31 |

**Table 5** Comparison of the sensing properties of $NH_3$ gas sensor based on different categories of nanocomposites sensors

| Sensor | Morphology | Gas concentration (ppm) | Operating temperature (°C) | Response time (s) | Recovery time (s) | Sensitivity | Reference |
|---|---|---|---|---|---|---|---|
| NiO-$SnO_2$ | Nanosphere | 20 | 300 | 0.5 | 4 | 60 | [35] |
| Sr-$SnO_2$ | Nanofibers | 2000 | RT | 6 | 10 | 55 | [36] |
| Pd-$SnO_2$-RGO | Nanoparticles | 100 | RT | 420 | 3000 | 19.6 | [37] |
| $SnO_2$-RGO | Nanorods | 200 | RT | 8 | 13 | 30 | [38] |
| $Co_3O_4$ | Hierarchical nanorods | 100 | 160 | 2 | 10 | 11.2 | [39] |
| $WO_3$ | Nanocrystal | 80 | 220 | 45 | 90 | 95 | [40] |
| $MnWO_4$ | Nanorods | 50 | 450 | 65 | 70 | 1.2 | [41] |
| $Ag_3PO_4$ | Nanoparticles | 100 | 50 | 276 | 1338 | 52 | [42] |
| Cu–ZnO | Nanorods | 100 | 150 | 5.5 | 55 | 32.3 | [43] |
| 70%$SnO_2$–30%CuO | Bucky particles | 150 | RT | 4 | 55 | 57% | This work |

**Acknowledgments** The authors would like to thank University of Technology, Baghdad-Iraq, Mustansiriyah University, Baghdad-Iraq, and University of Tehran, Tehran-Iran, for their support in the present work.

## References

1. X. Li, X. Li, Z. Li, J. Wang, J. Zhang, $WS_2$ nanoflakes based selective ammonia sensors at room temperature. Sens. Actuators B Chem. **240**, 273–277 (2017)
2. C.-T. Lee, Y.-S. Wang, High-performance room temperature $NH_3$ gas sensors based on polyaniline-reduced graphene oxide nanocomposite sensitive membrane. J. Alloy. Compd. **789**, 693–696 (2019)
3. A.M. Alwan, A.B. Dheyab, A.J. Allaa, Study of the influence of incorporation of gold nanoparticles on the modified porous silicon sensor for petroleum gas detection. Eng Technol J **35**, 811–815 (2017)
4. A. Sharma, P. Bhojane, A.K. Rana, Y. Kumar, P.M. Shirage, Mesoporous nickel cobalt hydroxide/oxide as an excellent room temperature ammonia sensor. Scripta. Mater. **128**, 65–68 (2017)
5. D.A. Hashim, A.M. Alwan, M.F. Jawad, Influence of Ag NPs on silicon nanocolumns $NH_3$ gas sensors. J. Electrochem. Soc. **165**, 773–778 (2018)
6. A.M. Alwan, A.B. Dheyab, Room temperature $CO_2$ gas sensors of AuNPs/mesoPSi hybrid structures. J. Appl. Nanosci. **7**, 335–341 (2017)
7. A.M. Alwan, R.A. Abbas, A.B. Dheyab, Study the Characteristic of planer and sandwich PSi gas sensor (Comparative Study). Silicon **10**, 2527–2534 (2018)
8. A.J. Kulandaisamy, J.R. Reddy, P. Srinivasan, K.J. Babu, G.K. Mani, P. Shankar, J.B.B. Rayappan, Room temperature ammonia sensing properties of ZnO thin films grown by spray pyrolysis: effect of Mg doping. J. Alloys Compd. **688**, 422–429 (2016)
9. S. Mubeen, M. Lai, T. Zhang, J. Lim, A. Mulchandani, M.A. Deshusses, N.V. Myung, Hybrid tin oxide-SWNT nanostructures based gas sensor. Electrochim. Acta **92**, 484–490 (2013)
10. A. Sharma, M. Tomar, V. Gupta, Low temperature operating $SnO_2$ thin film sensor loaded with $WO_3$ micro-discs with enhanced response for $NO_2$ gas. Sens. Actuators B **161**, 1114–1118 (2012)
11. A. Chowdhuri, V. Gupta, K. Sreenivas, Fast response $H_2S$ gas sensing characteristics with ultra-thin CuO islands on sputtered $SnO_2$. Sens. Actuators B **93**, 572–579 (2003)
12. N.V. Toan, N.V. Chien, N.V. Duy, D.D. Vuong, N.H. Lam, N.D. Hoa, N.V. Hieu, Scalable fabrication of $SnO_2$ thin films sensitized with CuO islands for enhanced $H_2S$ gas sensing performance. Appl. Surf. Sci. **324**, 280–285 (2015)
13. A. Sharma, M. Tomar, V. Gupta, Enhanced response characteristics of $SnO_2$ thin film based $NO_2$ gas sensor integrated with nanoscaled metal oxide clusters. Sens. Actuators B **181**, 735–742 (2013)
14. L.A. Patil, D.R. Patil, Heterocontact type CuO-modified $SnO_2$ sensor for the detection of a ppm level $H_2S$ gas at room temperature. Sens. Actuators B **120**, 316–323 (2006)
15. A. Kumar, A. Sanger, A. Kumar, R. Chandra, Highly sensitive and selective CO gas sensor based on a hydrophobic $SnO_2$/CuO bilayer. Royal Society of Chemistry **6**, 47178–47184 (2016)
16. T.-T. Li, R.-R. Zheng, Yu. Hui, Y. Yang, T.-T. Wang, X.-T. Dong, Synthesis of highly sensitive disordered porous $SnO_2$ aerogel composite material by the chemical deposition method: synergistic effect of a layer of CuO thin film. R. Soc. Chem. **7**, 39334–39340 (2017)
17. N.S.A. Eom, H.B. Cho, Y. Song, G.M. Go, J. Lee, Y.H. Choa, Room-temperature $H_2S$ gas sensing by selectively synthesized $Cu_x$ (x= 1, 2) O: $SnO_2$ thin film nanocomposites with oblique & vertically assembled $SnO_2$ ceramic nanorods. Sens. Actuators B Chem. **273**, 1054–1061 (2018)
18. Z. Bo, X. Wei, X. Guo, H. Yang, S. Mao, J. Yan, K. Cen, $SnO_2$ nanoparticles incorporated CuO nanopetals on graphene for high-performance room-temperature $NO_2$ sensor. Chem. Phys. Lett. **750**, 137485 (2020)
19. M. Li, Hu. Ming, P. Zeng, S. Ma, W. Yan, Y. Qin, Effect of etching current density on microstructure and $NH_3$-sensing properties of porous silicon with intermediate-sized pores. Electrochim. Acta **108**, 167–174 (2013)
20. M. Li, M. Hu, Q. Liu, S. Ma, P. Sun, Microstructure characterization and $NO_2$-sensing properties of porous silicon with intermediate pore size. Appl. Surf. Sci. **268**, 188–194 (2013)
21. A.A. Yousif, A.M. Alwan, H.R. Abed, Optimizing of macro porous silicon morphology for creation of $SnO_2$/CuO nanoparticles. AIP Conf. Proc. **2213**(1), 020004 (2020)
22. A.M. Alwan, A.A. Yousif, L.A. Wali, A study on the morphology of the silver nanoparticles deposited on the n-type porous silicon prepared under different illumination types. Plasmonics **13**, 1191–1199 (2017)
23. R.A. Ismail, A.M. Alwan, A.S. Ahmed, Preparation and characteristics study of nano-porous silicon UV photodetector. Appl Nanosci **7**, 9–15 (2016)
24. A. Majid, T. James, S. Argue, D. Kingston, M. Post, J. Margeson, G.J. Gardner, Characterization of CuO phase in $SnO_2$–CuO

prepared by the modified Pechini method. J. Sol-Gel Sci. Technol. **53**(2), 390–398 (2010)
25. A.M. Alwan, A.J. Allaa, Design and fabrication of nanostructures silicon photodiode. Mod. Appl. Sci. **5**, 106–112 (2011)
26. H.R. Abed, A.M. Alwan, A.A. Yousif, N.F. Habubi, Efficient $SnO_2$/CuO/porous silicon nanocomposites structure for $NH_3$ gas sensing by incorporating CuO nanoparticles. Opt. Quant. Electron. **51**, 1–13 (2019)
27. B.A. Latefa, S. Naama, A. Keffous, A. Hassein-Bey, T. Hadjesi, $H_2$ sensing properties of modified silicon nanowires. Prog. Natl. Sci. Mater. Int. **25**(2), 101–110 (2015)
28. M.V. Nguyen, N.D. Chinh, B.T. Huy, Y.-I. Lee, CuO-decorated ZnO hierarchical nanostructures as efficient and established sensing materials for $H_2S$ gas sensors. Sci. Rep. **6**(1), 1–13 (2016)
29. J. Liu, Lu. Yiting, X. Cui, Y. Geng, G. Jin, Z. Zhai, Gas-sensing properties and sensitivity promoting mechanism ofCu-added SnO2thin films deposited by ultrasonic spray pyrolysis. Sens. Actuators B Chem. **248**, 862–867 (2017)
30. L. Hou, C. Zhang, L. Li, Du. Cheng, X. Li, X.-F. Kang, W. Chen, CO Gas sensors based on p-type CuO nanotubes and CuO nanocubes: morphology and surface structure effects on the sensing performance. Talanta **188**, 41–49 (2018)
31. A.H. Min, H.-J. Kim, H.C. Lee, J.-S. Park, H.-N. Lee, Effects of porosity and particle size on the gas sensing properties of $SnO_2$ films. Appl. Surf. Sci. **481**, 133–137 (2019)
32. Z.S. Hosseini, A. Irajizad, A. Mortezaali, Room temperature $H_2S$ gas sensor based on rather aligned ZnO nanorods with flower-like structures. Sens. Actuators B Chem. **207**, 865–871 (2015)
33. F. Mohd-Yasin, D.J. Nagel, C.E. Korman, Noise in MEMS. Meas. Sci. Technol. **21**(1), 012001 (2009)
34. A.M. Alwan, D.A. Hashim, M.F. Jawad, Efficient bimetallic nanoparticles embedded-porous silicon CO gas sensor. Solid State Electron. **153**, 37–45 (2019)
35. L. Wang, J. Deng, T. Fei, T. Zhang, Template-free synthesized hollow NiO–$SnO_2$ nanospheres with high gas-sensing performance. Sens. Actuators B Chem. **164**, 90–95 (2012)
36. S. Xu, K. Kan, Y. Yang, C. Jiang, J. Gao, L.Q. Jing, P.K. Shen, L. Li, K.Y. Shi, Enhanced $NH_3$ gas sensing performance based on electrospun alkaline-earth metals composited $SnO_2$ nanofibers. J. Alloy. Comp. **618**, 240–247 (2015)
37. P.G. Su, L.Y. Yang, $NH_3$ gas sensor based on Pd/$SnO_2$/RGO ternary composite operated at room-temperature. Sens. Actuators B: Chem. **223**, 202–208 (2016)
38. Y. Chen, W. Zhang, Q.S. Wu, A highly sensitive room-temperature sensing material for NH3: $SnO_2$-nanorods coupled by rGO. Sens. Actuators B: Chem. **242**, 1216–1226 (2017)
39. J.N. Deng, R. Zhang, L.L. Wang, Z. Lou, T. Zhang, Enhanced sensing performance of the $Co_3O_4$ hierarchical nanorods to $NH_3$ gas. Sens. Actuators B Chem. **209**, 449–455 (2015)
40. M. Takács, C. Dücso, A.E. Pap, Fine-tuning of gas response by modification of nano-crystalline $WO_3$ layer morphology. Sens. Actuators B Chem. **221**, 281–289 (2015)
41. D.D. Trung, N.D. Cuong, K.Q. Trung, T.-D. Nguyen, N. Van Toan, C.M. Hung, N. Van Hieu, Controlled synthesis of manganese tungstate nanorods for highly selective $NH_3$ gas sensor. J. Alloys Compd. **735**, 787–794 (2018)
42. F. Yan, G. Shen, Xi. Yang, T. Qi, J. Sun, X. Li, M. Zhang, Low operating temperature and highly selective $NH_3$ chemiresistive gas sensors based on $Ag_3PO_4$ semiconductor. Appl. Surf. Sci. **479**, 1141–1147 (2019)
43. R.S. Ganesh, E. Durgadevi, M. Navaneethan, V.L. Patil, S. Ponnusamy, C. Muthamizhchelvan, S. Kawasaki, P.S. Patil, Y. Hayakawa, Tuning the selectivity of $NH_3$ gas sensing response using Cu-doped ZnO nanostructures. Sens. Actuators A Phys. **269**, 331–341 (2018)